Elsevier Editorial System(tm) for Geomorphology
Manuscript Draft

Manuscript Number:

Title: High-precision levelling, DInSAR and geological effects in the 2012 Emilia epicentral area

Article Type: Research Paper

Keywords: geodetic data, coseismic deformation, SAR interferometry, levelling, site effects

Corresponding Author: Prof. Riccardo Caputo,

Corresponding Author's Institution: University of Ferrara

First Author: Riccardo Caputo

Order of Authors: Riccardo Caputo; Alberto Pellegrinelli; Christian Bignami; Alessandro Bondesan; Ambra Mantovani; Salvatore Stramondo; Paolo Russo

Abstract: In May 2012, two moderate earthquakes (Mw = 6.1 and 5.9), associated with a noticeable aftershock sequence affected the eastern sector of the Po Plain, northern Italy. As far as the coseismic areal uplift events are crucial for better understanding the seismotectonics of the broader area and therefore for better assessing the seismic hazard of the region, in the present research, we analyze and compare the results of high precision levelling, DInSAR technique, the distribution of the liquefaction occurrences, the geomorphological map of the area and the structural model of the region. The DInSar technique points out a remarkable upflit of the ground (up to 17 cm), which was confirmed by high precision leveling. The results from both techniques are substantially in good agreement, even if some considerable discrepancies occur, probably due to a well documented and diffuse liquefaction phenomena.

Suggested Reviewers: Pierre Briole
briole@ens.fr
Expert in InSAR analysis and modeling applied to active tectonics

Michael Foumelis
Michael.foumelis@esa.int
Expert in InSAR processing

Alessandro Capra
alessandro.capra@unimore.it
Expert in surveying, in Geomatics, and in integrated systems for landslide monitoring. Editor in Chief of the international Journal “Applied Geomatics”

Athanasios Ganas
aganas@gein.noa.gr
expert in active tectonics and remote sensing

Iannis Koukouvelas
iannis@upatras.gr
expert in earthquake geology and morphogenic effects

High-precision levelling, DInSAR and geological effects in the 2012 Emilia epicentral area

Caputo R.[1,*], Pellegrinelli A.[2], Bignami C.[3], Bondesan A.[4], Mantovani A.[1], Stramondo S.[3], Russo P.[2]

1) Dept. of Physics and Earth Sciences, University of Ferrara, Italy

2) Dept. of Engineering, University of Ferrara, Italy

[3]) Istituto Nazionale di Geofisica e Vulcanologia, Rome, Italy

4) Consorzio di Bonifica Pianura di Ferrara, Ferrara, Italy

*) corresponding author (+39.0532.974688; rcaputo@unife.it)

Abstract

In May 2012, two moderate earthquakes (Mw = 6.1 and 5.9), associated with a noticeable aftershock sequence affected the eastern sector of the Po Plain, northern Italy. As far as the coseismic areal uplift events are crucial for better understanding the seismotectonics of the broader area and therefore for better assessing the seismic hazard of the region, in the present research, we analyze and compare the results of high precision levelling, DInSAR technique, the distribution of the liquefaction occurrences, the geomorphological map of the area and the structural model of the region. The DInSar technique points out a remarkable upflit of the ground (up to 17 cm), which was confirmed by high precision leveling. The results from both techniques are substantially in good agreement, even if some considerable discrepancies occur, probably due to a well documented and diffuse liquefaction phenomena.

keywords: geodetic data, coseismic deformation, SAR interferometry, levelling, site effects.

Introduction

In May 2012, two moderate (M_w = 6.1 and 5.9; *e.g.* Pondrelli *et al.*, 2012) earthquakes, associated with a noticeable aftershock sequence (*e.g.* Saraò and Peruzza, 2012; Scognamiglio *et al.*, 2012), affected the eastern sector of the Po Plain, Italy. The causative faults are two segments of the Ferrara Arc thrust system representing the frontal most portion of the buried Northern Apennines fold-and-thrust belt (Figure 1). In particular, the two major structures which were reactivated have a left-stepping largely overlapping geometry. Both seismogenic sources were associated with blind, mainly dip-slip reverse, faulting (*e.g.* Scognamiglio *et al.*, 2012; Pondrelli *et al.*, 2012), while the uppermost tip segment of the sliding planes has been estimated to reach a minimum depth of 3-4 km (Bignami *et al.*, 2012). As a consequence of the fault geometry and kinematics, the rock volume above the coseismic rupture tip was characterised by a typical fault-propagation folding process that eventually caused the bending of the topographic surface and the consequent uplift of the broader epicentral area (Bignami *et al.*, 2012; Salvi *et al.*, 2012).

Notwithstanding the high sedimentation rate characterizing the Po Plain, the repeating of similar 'areal morphogenic earthquakes' (Caputo, 2005) during Late Pleistocene and Holocene locally caused cumulative effects in the coeval stratigraphic succession, but also in the present-day morphology of the region. Although such stratigraphic lateral variations are relatively evident in the deeper geology (Pieri and Groppi, 1981; Boccaletti *et al.*, 2004), they are morphologically subtle in the otherwise flat topography of the alluvial plain and they could be emphasized only by a careful inspection of the hydrographic network, which however highlights the occurrence of several drainage anomalies (*e.g.* Burrato *et al.*, 2003; 2012). Indeed, such hydrographic anomalies were considered key features for documenting the recent tectonic activity of the underlying faults (Basili *et al.*, 2008; DISS WG, 2010) whose instrumental seismic record is generally poor likely due to the long recurrence intervals on these structures.

As far as these coseismic areal uplift events are crucial for better understanding the seismotectonics of the broader area and therefore for better assessing the seismic hazard of the region, in the present research we analyse in detail the geodetic available information relative to the May 2012 Emilia

51 earthquakes and compare the results from two different techniques, namely a high-precision levelling
52 and Differential Synthetic Aperture Radar interferometry (DInSAR; Massonnet *et al.*, 1993)
53 technique. We will first briefly recall the principles of the two approaches, discuss the independently
54 obtained results and then compare them in order to emphasize their pros and cons and the
55 complementarity of the two methods.
56

Hydrographic and morphological evolution of the western Ferrara plain

The present-day morphology of the western Ferrara plain is a direct result of the competition between high depositional rates, tectonic activity and differential compaction, as well as the latest Pleistocene-Holocene climate variations. These natural phenomena basically caused differential vertical movements which governed the recent hydrographic evolution and a highly variable sedimentary distribution, both lateral and vertical. As a consequence, the alluvial plain is actually crossed by few major and minor water courses, but it is characterised by many abandoned river channels and widespread flooding deposits. All these sedimentary bodies generally represent distinct morphological features which altimetrically outstand from the otherwise flat territory. Their topographic evidence (up to several meters) is commonly proportional to the channel importance and to their age. However, since the last two millennia, anthropogenic activities also played a role in the territory evolution.

As a first approximation, the western sector of the Ferrara plain consists of an ENE gently dipping topographic surface ranging between 20 m a.s.l. in the Cento area and ca. 4 m East of Ferrara. The mean slope is about 0.5‰, but where local topographic 'anomalies' occur associated with active or abandoned levees or breaches, the topographic gradient could be as high as 5%.

At ca 2500 years ago, the lowest sector of the Po River was flowing across the present-day Ficarolo, Bondeno, Ferrara and Cona, forming the socalled *Po di Ferrara* (*a* in Figure 2). In the same period, which was characterized by a generally warm climate, the Reno River was flowing across the present-day San Pietro and Poggio Renatico (*b* in Figure 2).

During the VI-VIII centuries A.D. the climate was particularly wet and the precipitations in the region were abundant (the socalled "deluge" as referred to by Paolo Diacono). This caused a hydrographic instability during which the Po di Ferrara splits into the *Volano* and *Primaro* (*c* and *d* in Figure 2, respectively) and at this bifurcation the first Ferrara settlement is established. In the same period (VI-VII centuries), the Reno River shifts westwards along a new course across Galliera (*e* in Figure 2), while after the XI century, it further jumps to the west flowing close to Pieve di Cento.

The restored warm conditions characterising the IX-XI centuries foster the farming expansion

within the plain, but during the XI century the eastern sector of the Po plain suffers the strongest hydrographic rearrangement historically documented associated with several disastrous flooding events near Ficarolo that induced the forming of a new major branch of the Po River (*Po Grande*) flowing north of Ferrara (*f* in Figure 2), which is still active today. This important territory reorganisation was likely caused by the reactivation of the Casaglia blind thrust, which is the frontalmost segment of the Ferrara Arc, and the growing of the associated fault-propagation anticline.

During the following centuries, the water discharge of the southern branches of the Po River, progressively decreased and hence the capacity of sediment transport. As a consequence, the river channels were filled with time causing increasingly frequent the flooding events and the development of a marsh area in the southern Ferrara territory. While the Panaro River continued to feed the Po of Ferrara near Bondeno (*g* in Figure 2), to the south the Reno River began to split into several channels, the major of which are that of Corpo Reno, Renazzo, Alberone and Bevilacqua (*h*, *i*, *l* and *m* in Figure 2, respectively), distributing water and sediments in a broad territory north of Cento (Bondesan *et al.*, 1992).

Following the disastrous flooding events of the 1451 and 1457 (Frizzi, 1848), the Reno River was artificially channeled running between Cento and Pieve (*n* in Figure 2) and it soon started to rapidly prograding several kilometers in just few years. Therefore, the course was more or less artificially extended towards Sant'Agostino and Vigarano Mainarda (*o* in Figure 2), where it was left to freely flood the area southwest of Ferrara and hence start filling these natural depressions. This hydrographic setting persisted for ca. 300 years and geographical stability allowed the establishment of new settlements like San Carlo and Mirabello. In 1526, this branch of the Reno River was connected to the Po of Ferrara by digging a channel NE of Vigarano (*p* in Figure 2) and this intervention turned out to be catastrophic for the Ferrara territory, due to the rapid sedimentary obstruction of the Po channel, that caused as many as 40 flooding events in just 16 year and the diffuse swamping of the area surrounding the town (Bottoni, 1873). Few decades later the Po di Ferrara was not able any more to drain the water of the Panaro affluent and at the end of the XVI century the flowing direction along this branch of the majojr river was reversed (*i.e.* from Bondeno to Ficarolo; Figure 2)

In the following century (XVII), the connection of Reno River into the Po di Ferrara was cut and

112 the former was diverted near Vigarano in a southeast direction (*q* in Figure 2) once more for inducing
113 a land reclamation by sedimentary infilling in the region between Ferrara and Poggio Renatico
114 (Roversi, 1989). At that time, the Po di Ferrara has completely lost its hydraulic dependence from the
115 present-day Po Grande and the worsening climatic conditions (*i.e.* increased precipitations, water
116 discharge and sediment transport) forced a progressive artificial elevation of the levees for many rivers
117 crossing the area and a hydrographic rearrangement. For example, in order to drain the swampy area
118 between Ferrara, Poggio Renatico and Malalbergo, in 1724-1742 was excavated the *Cavo Benedettino*
119 (*r* in Figure 2) partially exploiting older river channels. While in order to impede further disastrous
120 flooding events near Sant'Agostino (Franceschini, 1983), the Reno River was definitely diverted
121 southeastwards in 1771-1775 by excavating a direct connection with the Cavo Benedettino (*s* in Figure
122 2). Due to altimetric differences, the inlet of the Po di Primaro (*d* in Figure 2) into the Cavo
123 Benedettino near Traghetto was thus closed and this caused the hydraulic death of the former channel.
124 In the meantime, the Panaro River between Finale Emilia and Bondeno was flowing along two
125 courses, a natural branch and a partially artificial channel (*g* and *t* in Figure 2, respectively), of which
126 the first was definitely abandoned at the end of the XIX century.
127

DInSAR technique

DInSAR technique is based on the exploitation of the phase component from two SAR images of the same area. Each SAR image is composed of a real and an imaginary part, or equivalently, each pixel in a SAR image has an amplitude component and a phase component. The latter is related to the satellite-to-target distance, which is composed of a large number of integer wavelengths and the measured fractional phase component. The result of the application of DInSAR is the so-called "interferogram", that is the pixel-to-pixel difference of the phase components of two SAR images covering the same area.

The interferometric phase Φ_{int} can be schematically split into five terms, the "flat Earth" component Φ_{f}, the topographic phase Φ_{topo}, the displacement phase Φ_{displ}, the atmospheric term Φ_{atm}, and the error phase Φ_{err} (Massonnet and Feigl, 1998). The first term deals with the SAR acquisition geometry and can be easily removed thanks to the very precise knowledge of the orbital position and trajectory. The topographic phase is related to the normal baseline that is the projection of the distance between the two positions of the satellite, looking at the same region at different times, onto the direction orthogonal to the Line Of Sight (hereafter LOS; *i.e.*, the line from the sensor to the target on surface). Finally, displacements occurring on the ground surface and causing changes in the sensor-to-ground distance result in the phase variation (Φ_{displ}). In order to highlight this phase change due to displacement, the "flat Earth" and the topographic terms have to be removed (the latter in general using an independently determined Digital Elevation Model). Actually, the name DInSAR refers to the technique applied to generate such topographically corrected interferograms. This technique measures the projection of the displacement vectors (North, East and Up components of three-dimensional surface displacements) along the satellite LOS. The interferogram is calculated as the modulo 2π phase difference, because of the nature of complex numbers. In order to obtain a LOS displacement map, the result of DInSAR should be moved from the wrapped, discontinuous, interference signal, to the unwrapped, continuous phase difference. Phase unwrapping is often a critical step in the estimation of ground displacement, and if an interferogram is strongly affected by noise, the lack of signal continuity (decorrelation) may introduce errors in the displacement values (unwrapping errors). Such

155 errors can sometimes be mitigated using independent observations, such as GPS, leveling data, or
156 other interferograms from different orbits or satellites.

157 In order to study the surface deformation caused by the May 20 and May 29 events, we applied
158 the DInSAR technique to two pairs of SAR images. The first image pair has been acquired by the
159 Canadian satellite RADARSAT-1, a C-band SAR, on descending orbit. The pre-event RADARSAT-1
160 image is dated May 12, 2012, few days before the first mainshock, while the second image has been
161 acquired on June 5. Hence the time span covered thus embraces the two main shocks and several
162 aftershoks including five events with M_w greater than 5. The RADARSAT-1 pair has a perpendicular
163 (spatial) baseline of 309 m and a temporal baseline of 24 days. The topographic phase contribution has
164 been removed by using the Shuttle Radar Topographic Mission (SRTM; Farr *et al.*, 2007) DEM. In
165 addition, aiming at increasing the signal-to-noise ratio to allow a more accurate unwrapping of the
166 phase, the Goldstein filter (Goldstein and Werner, 1998) has been applied.

167 The resulting deformation map (Figure 3a) shows a region characterized by a movement toward
168 the satellite (an uplift) that reaches a maximum displacement of about 17 cm in LOS direction, which
169 in this case corresponds to 34° off nadir viewing angle. Two connected and partially overlapping
170 sectors within the investigated area show a marked displacement which is a clear effect of the (mainly)
171 coseismic activity of the two causative faults associated with the May 20 (eastern sector, $M_w = 6.1$)
172 and May 29 (western sector, $M_w = 5.9$) mainshocks. A relative small subsidence (up to a peak value of
173 about -3 cm) is also detected in the southern area close to the western sector.

174 A second SAR image pair, also on descending orbit, has been available from the Italian X-band
175 SAR mission COSMO-SkyMed. The two images are respectively dated May 19 and May 23, 2012,
176 hence with 4 days temporal separation and a perpendicular baseline of 366 m. It is noteworthy that the
177 latter image pair encompasses only the first of the two main shocks.

178 Also for COSMO-SkyMed data, the interferometric phase component related to the topography
179 has been removed by using the SRTM DEM, and the Goldstein filter has been applied to recover the
180 loss of interferometric coherence due to local effects, such as the occurred liquefactions. With this
181 approach we were able to keep the tectonic and large scale topographic deformation.

182 Figure 3b shows the displacement map obtained from the DinSAR processing of the COSMO-

SkyMed images. As observed in the RADARSAT-1 interferogram, a region with a maximum positive movement (toward the satellite) in LOS direction of about 13 cm is detected. The lower displacement with respect to the RADARSAT-1 interferogram is partly due to the fact that the COSMO-SkyMed data frame covers only the eastern sector of the epicentral area of the May 20 event, missing the sector characterised by the larger values. However, taking into account the different time span considered in the second interferogram, the larger surface displacement inferred from the RADARSAT-1 could be partly due to a prolonged post-seismic deformation effect.

High-precision levelling

The territory of the Ferrara Provinceis characterized by a low mean ground elevation a.s.l. and, for large sectors, even below the sea level. As above mentioned, for centuries human activities in this area have been guaranteed by carrying out several and continuous drainage works. Also today, an accurate knowledge of the topography of the area is a crucial information for a better drainage management.. For this purpose many years ago several permanent levelling networks were established in the whole province territory The creation of a network of such points and their repeated measurements represent the principal 'mission' of the "Consorzio di Bonifica Pianura di Ferrara" (hereinafter: “Consortium”) which dedicated to these activities the Geographic Information Sistem Sector.Between 2005 and 2012 a "First order" geometric levelling network covering the whole area of duty has been realized. The netwok provides a local vertical datum of high accuracy and consists of about 1,200 km of levelling lines across the Ferrara Province with an average length of levelling sections of about 1 km.

For the survey of the network, we met the international standards for high-precision geometric levelling. In particular, it was established a maximum allowed discrepancy of $\pm 2.5 \sqrt{\ell}$ mm in double-run levelling (where ℓ is the length of the levelling segment in km) and a maximum value for ring closure of $\pm 2.5 \sqrt{L}$ mm (where L is the length of the ring in km).

Since the first results from DInSAR (Bignami *et al.*, 2012; Salvi *et al.*, 2012) relative to the two major 2012 Emilia earthquakes, a significant and wide uplift of the ground was recognised (Figure 3). The eastern sector of the area affected by uplift is crossed by the levelling network of the Consortium and for the purpose of this research we carried out a dedicated survey along selected lines for a total length of about 120 km (Figure 4) in the months following the seismic crisis (September 2012-June 2013).

The levelling network has been measured using two digital levels Topcon DL101C with INVAR staffs (standard deviations 0.4 mm/km in double-run levelling). The adjustment of the measurements is performed by the classical least squares method. The resulting standard error of the adjusted heights' difference is ±1.14 mm/km, while the standard deviations of the adjusted heights is less than 5 mm.

The reference benchmark (point "A" in Figure 4) belongs to the Italian First Order Levelling

218 Network and were recently (2005) surveyed by IGM (Istituto Geografico Militare). Accordingly, all
219 the heights are referred to the national vertical datum. Considering that the Ferrara national
220 benchmark, which was precisely re-determined in 2005, is at an epicentral distance of ca. 25 km and
221 no permanent coseismic deformation has been never recorded for similar magnitude events at such
222 distances, we assumed its height as the vertical datum. On the other hand, also DInSAR technique
223 confirms the lack of detectable vertical deformation at the Ferrara site (see previous chapter and
224 Figure 3). The assumption of a 'stable' benchmark is likely further constrained by the fact that the
225 height of all secondary benchmarks of the levelling line closer to the reference benchmark (Ferrara)
226 remained almost unchanged comparing the measurements pre- and post-earthquakes (Figure 5).

227 In this datum, the heights of the benchmarks were compared obtaining the vertical movements of
228 the ground, occurred during the time interval between the two high-precision levelling campaigns
229 carried out before and after the seismic sequence.

230 The analysis of the vertical movements documented by high-precision levelling reveals the
231 occurrence of both uplifted and subsided benchmarks. The levelling lines which were re-measured
232 after the seismic sequence could be grouped into 3 main sets on the basis of their different orientation
233 and location as well as different behaviour in terms of vertical recorded movements. For example, the
234 three levelling lines closer to Ferrara (*i.e.* farest from the epicentre), with a mean E-W orientation
235 (Figure 5) show in practice a remarkable stability in time. Only the western part of the D-E line, which
236 is relatively closer to the epicentral area, suggests a slight, but systematic, uplift of 1-2 cm. Few
237 appreciable exceptions to this otherwise regular distribution of vertical movements occur near
238 Mirabello (Figure 5a,b) where a marked subsidence (up to ca. 10 cm) has been measured. The
239 behaviour of these benchmarks will be discussed in the following section.

240 A second set of levelling lines is represented in Figure 6 corresponding to three paths closer to the
241 epicentral area with a mean ESE-WNW orientation, threfore roughly parallel to the seismogenic fault's
242 strike associated with the areal morphogenic event of the 20th of May. Also in this case, we observe a
243 uniform behaviour of the single levelling lines, though variable from north to south. Indeed, the
244 northern line (C-B in Figure 6) documents no vertical movements, the southern one (G-H in Figure 6)
245 shows a slight subsidence of ca. 2 cm all along its length, while the intermediate one (F-D in Figure 6)

246 clearly indicates a general uplift ranging between 3 and 6 cm. This general picture characterised by
247 vertical stability in an ESE-WNW direction and lateral variations in a NNE-SSW direction is also
248 clearly emphasized by the levelling line G-F-C (Figure 7a), where the maximum uplift values have
249 been observed. The vertical movement of the benchmarks gradually vary along this line showing a
250 slight subsidence in the southern sector (1-2 cm), smoothly inverted in the central sector south of
251 Finale Emilia becoming a positive vertical movement (*i.e.* uplift) that progressively increases up to the
252 maximum value reached at about the km 15 (north of Finale Emilia). Farther northwards, the
253 displacement of the benchmarks specularly decreases to a few centimeters of uplift at Bondeno (Figure
254 7a). If we project the obtained values along a NNE-SSW straight line, it is possible to estimate a
255 wavelength of about 10 km for the fold deforming the topography.
256

Liquefaction and local subsidence

The May 2012 Emilia events have been characterized by spectacular and locally very intense liquefaction phenomena (*e.g.* Papathanassiou *et al.*, 2012; Caputo and Papathanassiou, 2012) that possibly mobilized shallow, but somewhere important, sedimentary volumes. As a consequence, ground deformations were induced at different scales involving areas from the few meters to several hundred meters in size and causing either horizontal movements up to several centimeters (*i.e.* lateral spreading), either vertical movements, both positive and negative; the latter generally much more frequent and locally exceeding some tens of centimeters. Such effects and especially their consequences on the Earth surface have occurred with a jeopardized pattern therefore influencing both terrestrial and satellite-based techniques, though in different ways.

As concerns the high-precision levelling, this effect is particularly manifest along the levelling line H-D-B (Figure 7b). Indeed, it runs parallel to the line G-F-C previously described showing both similarities and marked differences. For example, similarities are observed in the southern and central sectors, where all the benchmarks from south to north are characterized by a quite constant subsidence value (ca. 2 cm), which progressively changes into positive vertical movements (up to 3 cm of uplift near Sant'Agostino). However, in contrast to the G-F-C line, instead of farther regularly uplifting northwards, as showed by SAR displacement, from Sant'Agostino (point D) onwards the benchmarks show highly variable amounts of vertical displacements with prevailing negative values (*i.e.* subsidence) locally as great as -11.4 cm between San Carlo and Mirabello (Figure 7b). It is worth noting that interferometric processing, as already discussed, has been done aiming at preserving the large-scale tectonic signal, therefore, these local subsidences were smoothed out. In order to explain i) these discrepancies with respect to the relatively close and parallel profile (G-F-C), ii) the locally high subsidence values observed (up to -11.4 cm) and iii) the very short wavelength of the vertical variations, we anaysed different possible causes.

Firstly, it must be remarked that the benchmarks displacement could include the effect of possible long-term vertical movements occurred in the time span between the two campaigns (2005-2012). However, the available data (http://www.arpa.emr.it/dettaglio_notizia.asp?id=4801&idlivello=1414, in

284 Italian, last visited April 28, 2014) suggest that the 'regional' subsidence affecting the broader region
285 of the lower Po Plain occurred during this time span, and also recorded at the reference benchmark of
286 Ferrara, should be less than 1 to 2 cm. Above all, for the concern of this paper, no significant gradients
287 have been documented so far within the investigated area. We could thus exclude a long-term effect as
288 the causative phenomenon for the observed local, but strongly, subsided benchmarks and the
289 difference betwen high-precision levelling and satellite interferometry results.

290 Secondly, we analysed in detail the geological setting of the sites where the 'anomalous'
291 benchmarks have been installed. Indeed, immediate post-event surveys following the May 20
292 earthquake largely documented diffuse liquefaction phenomena in this sector of the plain (Figure 2;
293 *e.g.* Papathanassiou *et al.*, 2012; Caputo and Papathanassiou, 2012).

294 Data providing information on the shallow subsoil close to each benchmark derive from drill
295 cores, penetration tests and water wells. Although we performed a similar analysis for all controversial
296 benchmarks, we will show and discuss here only few remarkable examples allowing to understand the
297 above mentioned 'anomalous' behaviour observed along the levelling line. For example, the
298 benchmark *78020* (yellow star in Figure 8a), located at the entrance of the Mirabello cemetery, was
299 affected by a subsidence of 11.4 cm (Figure 7b). The cemeterial area is located along a palaeo-branch
300 of the Reno River (location *o* in Figure 2) and particularly at the base of the sotheastern slope of the
301 left levee (Figure 8a). The shallow stratigraphy observed in some drill cores carried out in the
302 surroundings of the benchmark (black stars in Figure 8a) consists of alternating fine silty sand and
303 saturated sandy silt in the first 5 to 6 m overlying a thick body of medium-grained sand. These
304 represent typical conditions prone to liquefaction in case of seismic shaking. As a matter of fact,
305 during the May 20 event, the cemetery broader area was affected by several ground effects associated
306 with, and induced by, widespread liquefaction phenomena. In particular, at few meters from the
307 benchmark *78020*, several ground deformations were coseismically formed (red squares in Figures 8a
308 and Figure 8d) clearly documenting the local loss of shear resistance within the subsoil that certainly
309 reacted differentially as a function of the vertical loads. At this regard, it is noteworthy that the
310 benchmark is cemented next to the heavy entrance pillar of the cemetery boundary wall, which very
311 likely suffered some amount of settling, therefore displacing also the benchmark. Moreover, large

312 amounts of liquefied sand was ejected within the broader area (blu dots in Figure 8a) and this
313 necessarily caused further subsidence due to the consequent compaction and volumetric reduction of
314 the underlying sandy layer(s). In addition to the 'local' effects, the whole southeastern slope of the
315 levee suffered a large-scale lateral spreading phenomenon (Figures 8a,b); the sliding surface has likely
316 exploited gently dipping sandy foresets well documented within the same levee body few kilometers
317 to the south within a palaeoseismological trench (Caputo *et al.*, 2012). Accordingly, the lateral
318 spreading also induced a vertical component of motion (Figure 8c), which certainly contributed to the
319 subsidence of benchmark *78020* (-11.4 cm). Similar phenomena have been also documented by Pizzi
320 and Scisciani (2012).

321 A second example is represented by the benchmark *78060*, located on the base of a tall lamppost
322 installed at the center of the roundabout at the northern entrance of San Carlo village (Figures 9a and
323 b). Drill-cores and cone penetration tests carried out few tens meters away from the benchmark clearly
324 show the presence of saturated fine silty sands between 4 to 6 m depth. Based on the CPTs, it is also
325 possible to calculate a Potential Liquefaction Index LPI (Iwasaki, 1978), with the approach proposed
326 by Idriss and Boulanger (2008), of 10.5 which corresponds to a high liquefaction risk (Sonmez, 2003).
327 Moreover, widespread sand ejections were observed in the surroundings by the immediate post-event
328 survey (Figure 9c; Caputo and Papathanassiou, 2012). Taking into account that the fundation consists
329 of roughly 1 m^3 of concrete and adding the weight of the metal pole to this punctual load, some
330 amount of permanent settling induced by the coseismic liquefaction would be expected and could
331 reasonably explain the 2.8 cm of subsidence measured at this benchmark (Figure 7b).

332 Again at San Carlo, the benchmark *78080* located on the bikes lane along the provincial road
333 (Figure 9a), was affected by 4.4 cm of subsidence (Figure 7b). Here also, CPTs carried out close to the
334 benchmark clearly document the occurrence of a saturated sandy silt layer between 4.5 to 5.5 m depth
335 and a moderate LPI value. Interestingly, few tens of meters away from the benchmark, a water well
336 has apparently been uplifted of ca. 8 cm, therefore coming out from its case (Figure 9e); considering
337 that the metal rod is rooted at 30 m-depth, more likely it was the nearby ground that has permanently
338 subsided as a consequence of the important amount of dewatering, sand ejection and hence compation
339 observed in the surroundings.

A final example is from the benchmark *78090* that suffered a subsidence of 5.3 cm (Figure 7b). Similar to the Mirabello case previously discussed (Figure 8), the benchmark is fixed at the entrance of a cemeterial area located along the same palaeo-branch of the Reno River (location *o* in Figure 2) though in this case at the base of the right levee external slope (Figure 9a). Here also lateral spreading and diffuse sand ejection phenomena have occurred in concomitance with the May 20 event (respectively white arrows and blu dots in Figure 9a), while geotechnical results and palaeoseismological excavations (Caputo *et al.*, 2012) confirm the presence of a thick layer of saturated fine-medium sands between 4 to 8-8.5 m depth. As a consequence both horizontal and vertical movements were induced (Figures 9d and 7b), therefore justifying the measured subsidence and allowing to classify this as a local effect.

Concluding remarks

In order to better exploit all available information on the ground motion, we compare the results of i) the high-precision levelling, ii) the DInSAR analyses, iii) the distribution of the 2012 liquefaction occurrences; iv) the geomorphological map of the area and v) the structural model of the region providing information about the depth of the bedrock.

The interferograms clearly define a large sector of the alluvial plain characterized by an elliptical geometry affected by a marked uplift. This occurs in correspondence with the crest of a fault-propagation fold associated with the causative source of the Emilia May 20 event. Satellite analyses also show two broad areas affected by a slight subsidence north and south of the anticline (Figure 3) in perfect agreement with elastic deformation models (*e.g.* Okada, 1985; Burrato *et al.*, 2003). By calculating the vertical movement from the LOS values, the maximum observed uplift is ca. 17 cm near Casumaro, while the amount of subsidence is everywhere smaller than 3 cm. Although the pair of RADARSAT-1 images embraces a time span including both major earthquakes, the area uplifted by the May 20 event is clearly recognisable and measures about 27 km in length and almost 10 km in width (ESE-WNW and NNE-SSW, respectively). This surface deformation has been also described and modelled by Pezzo *et al.* (2013).

As far as the Cosmo-SkyMed 'captures' only the first earthquakes while the RADARSAT-1 both events, we also attempted to analyse the possible effects accumulated during the post-seismic deformation of the first major shock. Taking into account the different quality of the imageries and characteristics of the two satellites, a comparison does not show the occurrence of post-seismic effects or at least the induced LOS variations were below the resolution of the two methods.

As stated above, one of the major aims of this research is represented by the comparison of the results of the high-precision levelling with those obtained from the satellite DInSAR. At this regard, it is possible to observe the perfect agreement in Figures 5, 6 and particularly 7a, where the pattern of vertical movements obtained from the two approches nicely mimic each other. It is also noteworthy that locally the two techniques are almost complementary. For example, along the profile G-F-C (Figure 7a) between Finale Emilia and Bondeno the satellite information is missing because the results

show no coherence. Conversely, along the profile H-D-B (Figure 7b), north of Sant'Agostino, several benchmarks of the levelling have been affected by local coseismic effects showing anomalous subsidence values which do not reflect the general, large-scale tectonically induced, surface deformation. In this case the satellite data fullfill the information gap.

A second major goal of this work is the comparison of our results with the tectonic setting of the region corresponding to the central-western part of the complex Ferrara Arc representing the frontal and buried sector of the Northern Apennines orogenic wedge. The uplifted areas documented in this paper clearly reflect the re-activation of blind thrusts representing distinct seismogenic segments and contribute constraining their geometry and kinematics. On the other hand, the cumulative Quaternary effects are also emphasized by the important lateral variations in thickness of the coeval deposits (*e.g.* Martelli and Molinari, 2008), while the most recent activity is suggested by the several hydrographic anomalies observed in the epicentral area (*e.g.* Burrato *et al.*, 2012), like the divergence of two palaeochannels near Finale Emilia (*g* and *l* in Figure 2), the progressive infilling and abandonment of the Sant'Agostino to Mirabello branch of the Reno River (*o* in Figure 2) and its older paths (*b* and *e* in Figure 2) as well as the recent avulsion (*s* in Figure 2), though anthropogenically forced.

As a final comment, we want to stress the lesson learned relative to the topology of high-precision levelling networks and particularly concerning the location of the benchmarks. Indeed, it is obvious that such monitoring systems must be located for practical reasons along major road axes, which however in alluvial plains have the disadvantage to commonly run on top of artificial embankments or natural levees. As a consequence, both earthworks and sedimentary bodies easily suffer diffuse settling and liquefaction effects in case of moderate-to-strong seismic shaking. If no alternative siting is available for locating high-precision levelling lines, network planners should be aware of the intrinsic risk of 'loosing' some benchmarks.

Acknowledgments

References

Basili R., Valensise G., Vannoli P., Burrato P., Fracassi U., Mariano S., Tiberti M.M. and Boschi E. (2008): The Database of Individual Seismogenic Sources (DISS), version 3: summarizing 20 years of research on Italy's earthquake geology. *Tectonophys.*, **453**(1-4), 20-43 doi:10.1016/j.tecto.2007.04.014

Bignami C., Burrato P., Cannelli V., Chini M., Falcucci E., Ferretti A., Gori S., Kyriakopoulos C., Melini D., Moro M., Novali F., Saroli M., Stramondo S., Valensise G. and Vannoli P. (2012): Coseismic deformation pattern of the Emilia 2012 seismic sequence imaged by Radarsat-1 interferometry. *Annals of Geophys.*, **55**(4), 788-795, doi: 10.4401/ag-6157.

Boccaletti M., Bonini M., Corti G., Gasperini P., Martelli L., Piccardi L., Tanini C. and Vannucci G. (2004): *Seismotectonic Map of the Emilia-Romagna Region, 1:250000*. Regione Emilia-Romagna – CNR.

Bondesan M., Ferri R., Graziani S. (1992): Aspetti geomorfologici e problemi paleogeografici della zona fra Bondeno, Finale Emilia e Mirabello nel quadro degli antichi domini idrografici del Secchia, del Panaro e del Reno. In: Gelichi S. (Ed.): *Un mito e un territorio: Ansalaregina e l'Alto Ferrarese nel Medioevo*, Ed. All'insegna del Giglio, Firenze, pp. 13-44.

Bottoni A. (1873): Appunti storici sulle rotte del basso Po dai tempi romani a tutto il 1839. Tip. Sociale, Ferrara.

Burrato P., Ciucci F. and Valensise G. (2003): An inventory of river anomalies in the Po Plain, northern Italy: evidence for active blind thrust faulting. *Annals of Geophys.*, **46**(5), 865-882.

Burrato P., Vannoli P., Fracassi U., Basili R. and Valensise G. (2012): Is blind faulting truly invisible? Tectonic-controlled drainage evolution in the epicentral area of the May 2012, Emilia-Romagna earthquake sequence (northern Italy). *Annals of Geophys.*, **55**(4), 525-531, doi: 10.4401/ag-6182.

Caputo R. (2005): Ground effects of large morphogenic earthquakes. *J. Geodyn.*, **40**(2-3), 113-118.

Caputo R. and Papathanasiou G. (2012): Ground failure and liquefaction phenomena triggered by the 20 May, 2012 Emilia-Romagna (Northern Italy) earthquake: case study of Sant'Agostino - San

431 Carlo - Mirabello zone. *Nat. Haz. Earth System Sciences*, **12**(11), 3177-3180, doi:10.5194/nhess-
432 12-3177-2012.
433 Caputo R., Iordanidou K., Minarelli L., Papathanassiou G., Poli M.E., Rapti-Caputo D., Sboras S.,
434 Stefani M. and Zanferrari A. (2012): Geological evidence of pre-2012 seismic events, Emilia-
435 Romagna, Italy. *Ann. Geophysics*, **55**(4), 743-749, doi: 10.4401/ag-6148.
436 C.N.R. (1992): *Structural Model of Italy*. Prog. Fin. Geodinamica, sottoprog. Modello strutturale
437 tridimensionale.
438 DISS Working Group (2010). Database of Individual Seismogenic Sources (DISS), Version 3.1.1: A
439 compilation of potential sources for earthquakes larger than M 5.5 in Italy and surrounding areas.
440 http://diss.rm.ingv.it/diss/, © INGV 2010 - Istituto Nazionale di Geofisica e Vulcanologia - All
441 rights reserved; doi:10.6092/INGV.IT-DISS3.1.1
442 Farr T.G., Rosen P.A., Caro E., Crippen R., Duren R., Hensley S. and Alsdorf D. (2007): The Shuttle
443 Radar Topography Mission. *Rev. Geophysics*, **45**(2). doi:10.1029/2005RG000183.
444 Franceschini A. (1983): Una storia di acque. In *Vigarano, Storia/Attualità*. Ferrara.
445 Frizzi A. (1848): Memorie per la storia di Ferrara.
446 Goldstein R.M.and Werner C.L. (1998): Radar interferogram filtering for geophysical applications.
447 *Geophys. Res. Letts.*, **25**(21), 4035-4038. doi:10.1029/1998GL900033
448 Idriss I.M. and Boulanger R.W. (2008): Soil liquefaction during earthquakes, *Earthquake Engineering*
449 *Research Institute MNO-12*.
450 Iwasaki T., Tatsuoka F., Tokia K.-i. and Yasuda S. (1978): A practical method for assessing soil
451 liquefaction potential based on case studies at various sites in Japan. 2nd Int. Conf. on
452 Microzonation, San Fancisco, *Proceedings*, 885-896.
453 Martelli L. and Molinari F.C. (2008): Studio geologico finalizzato alla ricerca di potenziali serbatoi
454 geotermici nel sottosuolo del comune di Mirandola. Regione Emilia-Romagna, Servizio Geologico,
455 Sismico e dei Suoli, Bologna.
456 Massonnet D., Rossi M., Carmona C., Adragna F., Peltzer G., Feigl K. and Rabaute T. (1993): The
457 displacement field of the Landers earthquake mapped by radar interferometry. *Nature*, **364**(6433),
458 138-142. doi:10.1038/364138a0

459 Massonnet D. and Feigl K.L. (1998): Radar interferometry and its application to changes in the
460 earth's surface. *Rev. Geophysics*, **36**(4), 441-500. doi:10.1029/97RG03139
461 M.U.R.S.T. (1997): *Carta Geomorfologica della Pianura Padana alla scala 1:250.000.* coord.
462 Castiglioni G.B., S.EL.CA., Firenze.
463 Okada Y. (1985): Surface deformation due to shear and tensile faults in a half-space. *Bull. Seism. Soc.*
464 *Am.*, **75**, 1135-1154.
465 Papathanassiou G., Caputo R. and Rapti-Caputo D. (2012): Liquefaction phenomena along the palaeo-
466 Reno River caused by the May 20, 2012 Emilia (Northern Italy) earthquake. *Ann. Geophysics,*
467 **55**(4), 735-742, doi: 10.4401/ag-6147.
468 Pezzo G., Merryman Boncori J.P., Tolomei C., Salvi S., Atzori S., Antonioli A., Trasatti E., Novali F.,
469 Serpelloni E., Candela L. and Giuliani R. (2013): Coseismic deformation and source modeling of
470 the May 2012 Emilia (Northern Italy) earthquakes. *Seismol. Res. Lett.*, **84**(4), 645-655, doi:
471 10.1785/0220120171.
472 Pieri M. and Groppi G. (1981): *Subsurface geological structure of the Po Plain, Italy*. Consiglio
473 Nazionale delle Ricerche, Progetto finalizzato Geodinamica, sottoprogetto Modello Strutturale,
474 pubbl. N° 414, Roma, 13 pp.
475 Pizzi A. and Scisciani V. (2012): The May 2012 Emilia (Italy) earthquakes: preliminary
476 interpretations on the seismogenic source and the origin of the coseismic ground effects. *Annals of*
477 *Geophys.*, **55**(4), 751-757, doi: 10.4401/ag-6171.
478 Pondrelli S., Salimbeni S., Perfetti P. and Danecek P. (2012): Quick regional centroid moment tensor
479 solutions for the Emilia 2012 (northern Italy) seismic sequence. *Annals of Geophys.*, **55**(4), 615-
480 621, doi: 10.4401/ag-6146.
481 Roversi R. (1989): Assetto idraulico del territorio ferrarese. in *Terre e acqua*, Corbo ed.
482 Salvi S., Tolomei C., Merryman Boncori J.P., Pezzo G., Atzori S., Antonioli A., Trasatti E., Giuliani
483 R., Zoffoli S. and Coletta A. (2012): Activation of the SIGRIS monitoring system for ground
484 deformation mapping during the Emilia 2012 seismic sequence, using COSMO-SkyMed InSAR
485 data. *Annals of Geophys.*, **55**(4), 796-802, doi: 10.4401/ag-6181.

Saraò A. and Peruzza L. (2012): Fault-plane solutions from moment-tensor inversion and preliminary Coulomb stress analysis for the Emilia Plain. *Annals of Geophys.*, **55**(4), 647-654, doi: 10.4401/ag-6134.

Scognamiglio L., Margheriti L., Mele F.M., Tinti E., Bono A., De Gori P., Lauciani V., Lucente F.P., Mandiello A.G., Marcocci C., Mazza S., Pintore S. and Quintiliani M. (2012): The 2012 Pianura Padana Emiliana seimic sequence: locations, moment tensors and magnitudes. *Annals of Geophys.*, **55**(4), 549-556, doi: 10.4401/ag-6159.

Sonmez, H. (2003): Modification of the liquefaction potential index and liquefaction susceptibility mapping for a liquefaction-prone area (Inegol, Turkey). *Environmental Geology* **44**(7), 862-871.

Veggiani A. (1972): Il ramo del Po di Adria nella tarda età del bronzo. *Padusa*, 3-4, pp. 123-136.

Figure captions

Figure 1: Tectonic framework of northern Italy, showing the buried Northern Apennines fold-and-thrust belt underlying the Po Plain and the major tectonic structures. Stars indicate the epicenters of two principal earthquakes of the May-June 2012 seismic sequence (May 20, M_L=5.9 and May 29, M_L=5.8). The box indicates the location of Figure 2.

Figure 2: Morphological map of the broader epicentral area showing the complex hydrographic drainage developped in historical times as a consequence of the tectonic activity, climate changes and anthropogenic management. See Figure 1 for location. Letters indicate distinct branches of the Po, Reno and Panaro rivers referred to in the text. Legend: 1) palaeo- and active levees associated with a morphological relief; 2) palaeo-channels entrenched in the alluvial plain; 3) flooding areas characterised by sandy deposits; 4) surface evidence of liquefaction phenomena caused by the May 20, 2012 event; 5) major breaches and associated fan deposits.

Figure 3: a) DInSAR results applied to the Canadian RADARSAT-1 satellite data (C-band SAR on descending orbit). The paired imageries analysed are respectively dated May 12 and June 5, 2012 and hence document the deformation associated with both mainshocks (May 20 and 29). Note the clear and distinct (though partially ovelapping) effects of the two principal morphogenic earthquakes. b) DInSAR results applied to the European COSMO-SkyMed -1 satellite data (X-band SAR on descending orbit). The paired imageries analysed are respectively dated May 19 and May 23, 2012 and hence document the deformation associated only to the first mainshock (May 20). The high-precision levelling lines discussed in this paper are also shown.

Figure 4: The first order levelling network belonging to the “Consorzio Pianura di Ferrara”, Province of Ferrara, which has been re-measured following the 2012 seismic sequence. Small dots represent the benchmarks of the Consortium, the exagons represent the labelled benchmarks discriminating

523 the levelling lines, while the triangle is the reference benchmark belonging to the Italian First Order
524 Levelling Network, recently (2005) re-surveyed by IGM (Istituto Geografico Militare).
525
526 Figure 5: Vertical movements measured along the three levelling lines closer to Ferrara (*i.e.* farest
527 from the epicentre), with a mean E-W orientation and showing a remarkable stability. The error bar
528 at each benchmark calculated on the basis of the standard deviations of the differences in elevation
529 (pre- to post-earthquake) is smaller than the symbol size. Capital letters refer to the benchmarks
530 labelled in Figure 4. HPL: high-precision levelling; RS1: RADARSAT-1; CSM: COSMO-
531 SkyMed.
532
533 Figure 6. Vertical movements measured along the three levelling lines closer to the epicentral area
534 with a mean ESE-WNW orientation showing a uniform behaviour of the single levelling lines,
535 though variable from north to south. he error bar at each benchmark calculated on the basis of the
536 standard deviations of the differences in elevation (pre- to post-earthquake) is smaller than the
537 symbol size. Capital letters refer to the benchmarks labelled in Figure 4. HPL: high-precision
538 levelling; RS1: RADARSAT-1; CSM: COSMO-SkyMed.
539
540 Figure 7: Vertical movements measured along the two levelling lines running perpendicular to the
541 May 20 fault strike. Profile G-F-C (a) perfectly reproduces the satellite results, while profile H-D-B
542 shows some marked differences with strongly subsided benchmarks. The error bar at each
543 benchmark calculated on the basis of the standard deviations of the differences in elevation (pre- to
544 post-earthquake) is smaller than the symbol size. Capital letters refer to the benchmarks labelled in
545 Figure 4. HPL: high-precision levelling; RS1: RADARSAT-1; CSM: COSMO-SkyMed.
546
547 Figure 8: a) GoogleEarth frame of Mirabello cemetery area showing the distribution of the secondary
548 coseismic effects, like sand ejection points (blue dots), ground deformation sites (red squares), drill
549 cores (black stars), ground ruptures (yellow arrows) and sliding direction due to lateral spreading
550 (white arrows). The yellow star indicates the location of benchmark *78020* characterised by 11.4

cm of subsidence. b) Ground ruptures observed on top of the abandoned levee (see (a) for location). c) Effects of the lateral spreading on the lateral wall of the cemetery (see (a) for location). d) Example of ground deformation associated with shallow liquefaction phenomena (see (a) for location).

Figure 9: a) Digital elevation model of the San Carlo area clearly showing the two levees of the palaeo-Reno River. Red lines represent the major ground ruptures observed after the May 20 event (Caputo and Papathanassiou, 2012) generally associated with lateral spreading phenomena (white arrows). Blu dots are san ejection points while black ones are penetration tests providing information about the shallow subsoil. Yellow stars are benchmarks of the high-precision levelling line. b) The foundations of the lamppost installed at the center of the roundabout at the northern entrance of San Carlo village where diffuse liquefaction has occurred (c) (see (a) for locations). d) The southern wall of the Sant'Agostino cemetery built on the slope of the palaeolevee and affected by lateral spreading thus contributing to the subsidence of benchmark *78090*. e) Example of water well located close to benchmark *78080*, which was apparently uplifted ca. 8 cm relative to the ground surface therefore coming out from its case. See text for discussion.

568

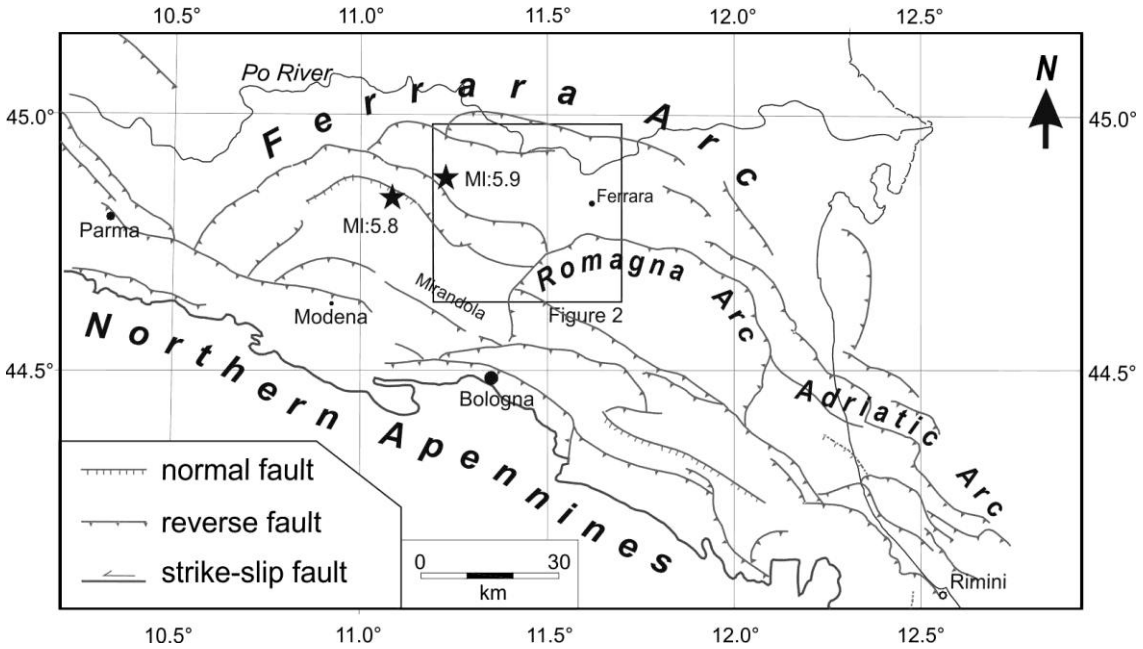

569

570

571 Figure 1

572

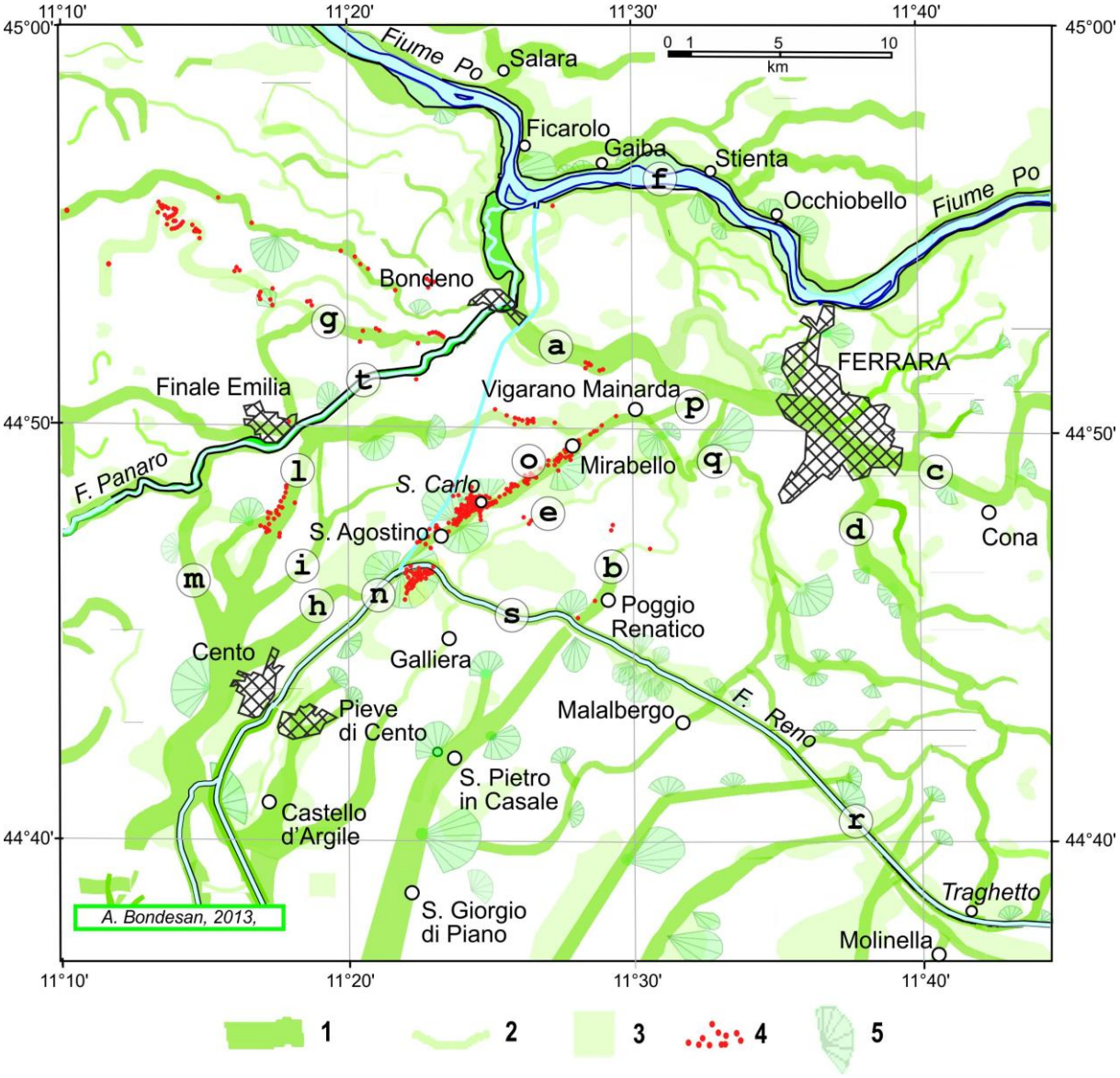

573

574 Figure 2

575

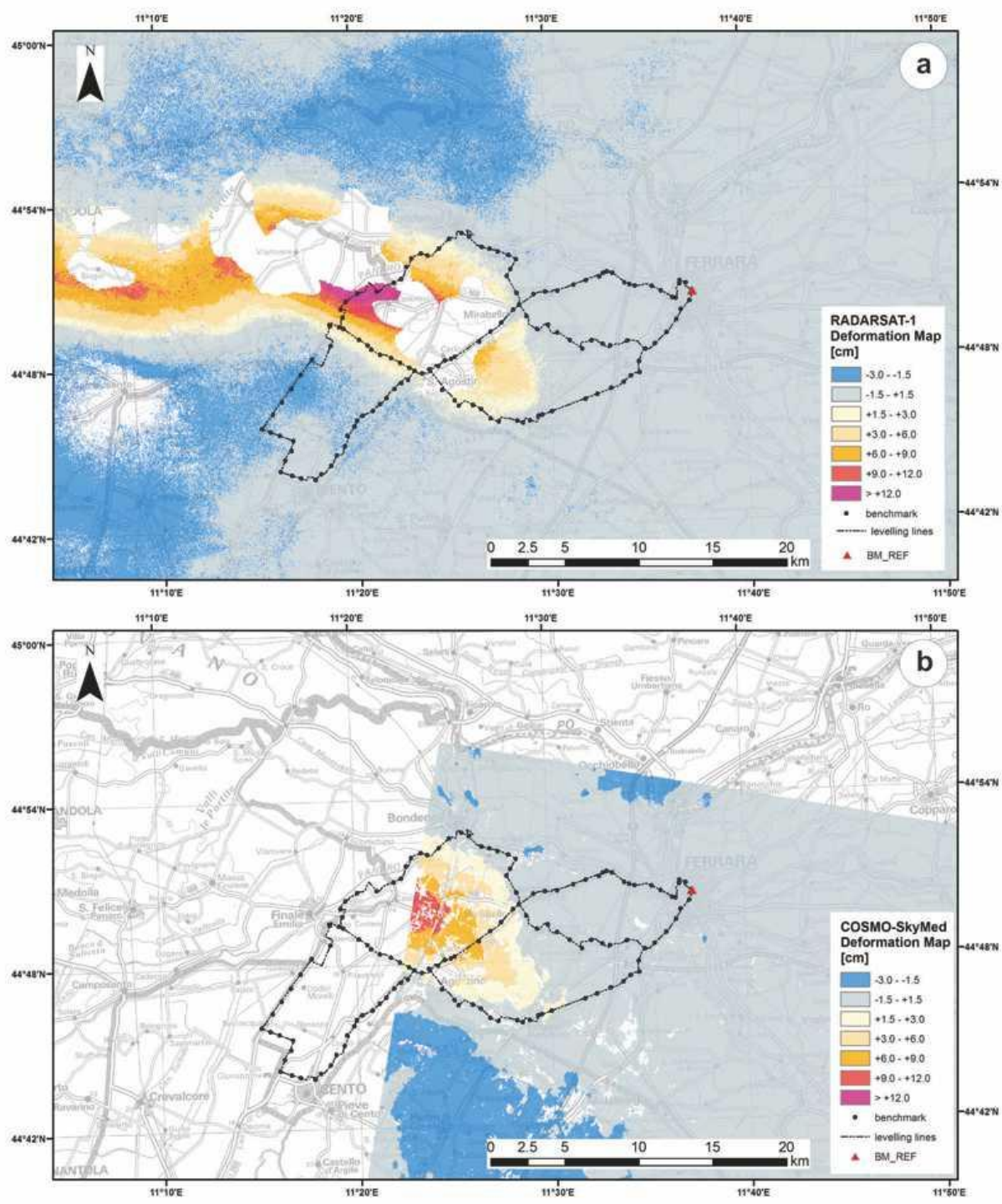
a
RADARSAT-1
Deformation Map
[cm]
-3.0 - -1.5
-1.5 - +1.5
+1.5 - +3.0
+3.0 - +6.0
+6.0 - +9.0
+9.0 - +12.0
> +12.0
benchmark
levelling lines
BM_REF
0 2.5 5 10 15 20
km
b
COSMO-SkyMed
Deformation Map
[cm]
-3.0 - -1.5
-1.5 - +1.5
+1.5 - +3.0
+3.0 - +6.0
+6.0 - +9.0
+9.0 - +12.0
> +12.0
benchmark
levelling lines
BM_REF
0 2.5 5 10 15 20
km

Figure 3

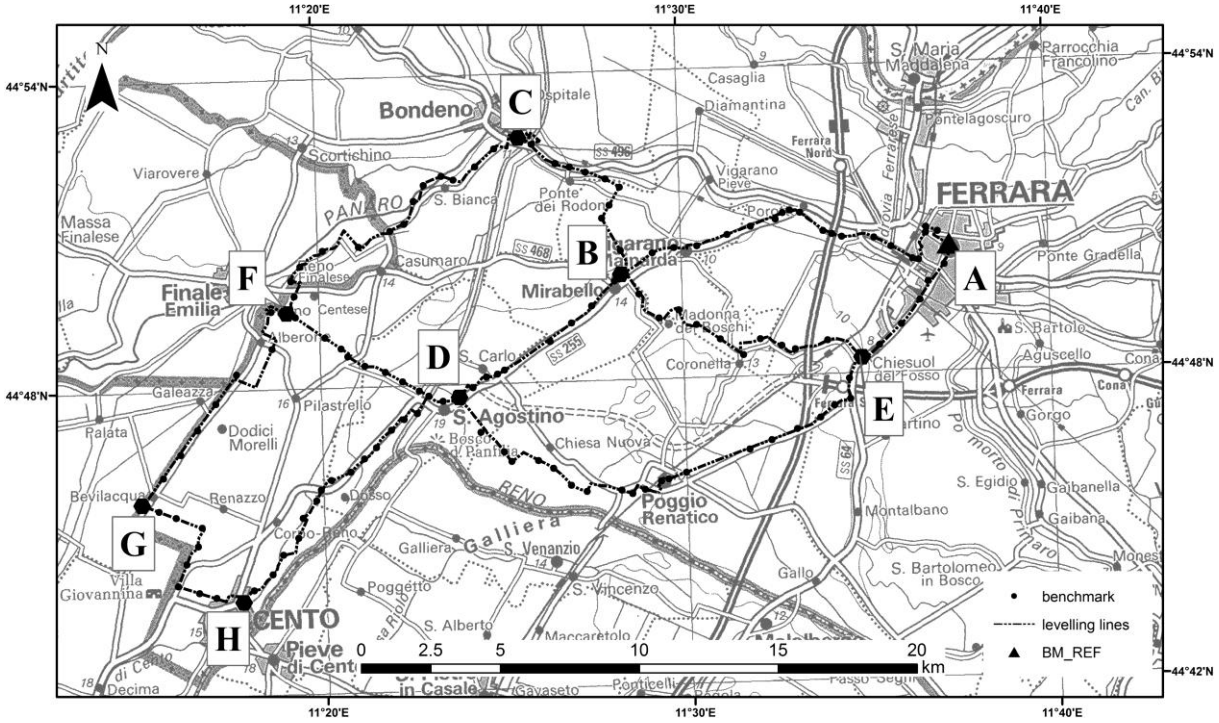
11°20'E
11°30'E
11°40'E
44°54'N
44°48'N
44°42'N
A
B
C
D
E
F
G
H
FERRARA
Bondeno
Finale Emilia
Mirabello
Poggio Renatico
S. Agostino
CENTO
Pieve di Cento
benchmark
levelling lines
BM_REF
0 2.5 5 10 15 20
km

Figure 4

583

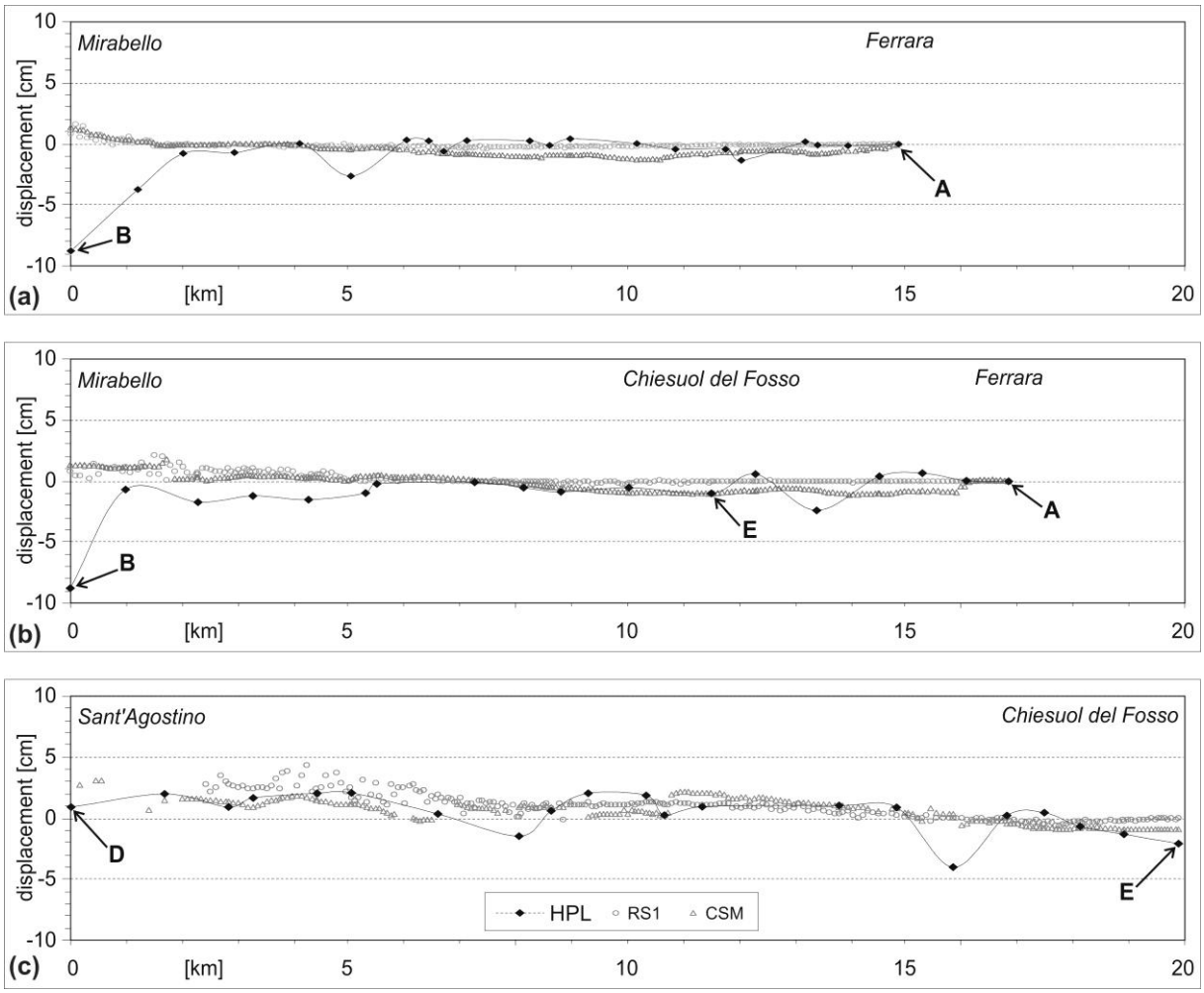

584

585

586 Figure 5

587

588

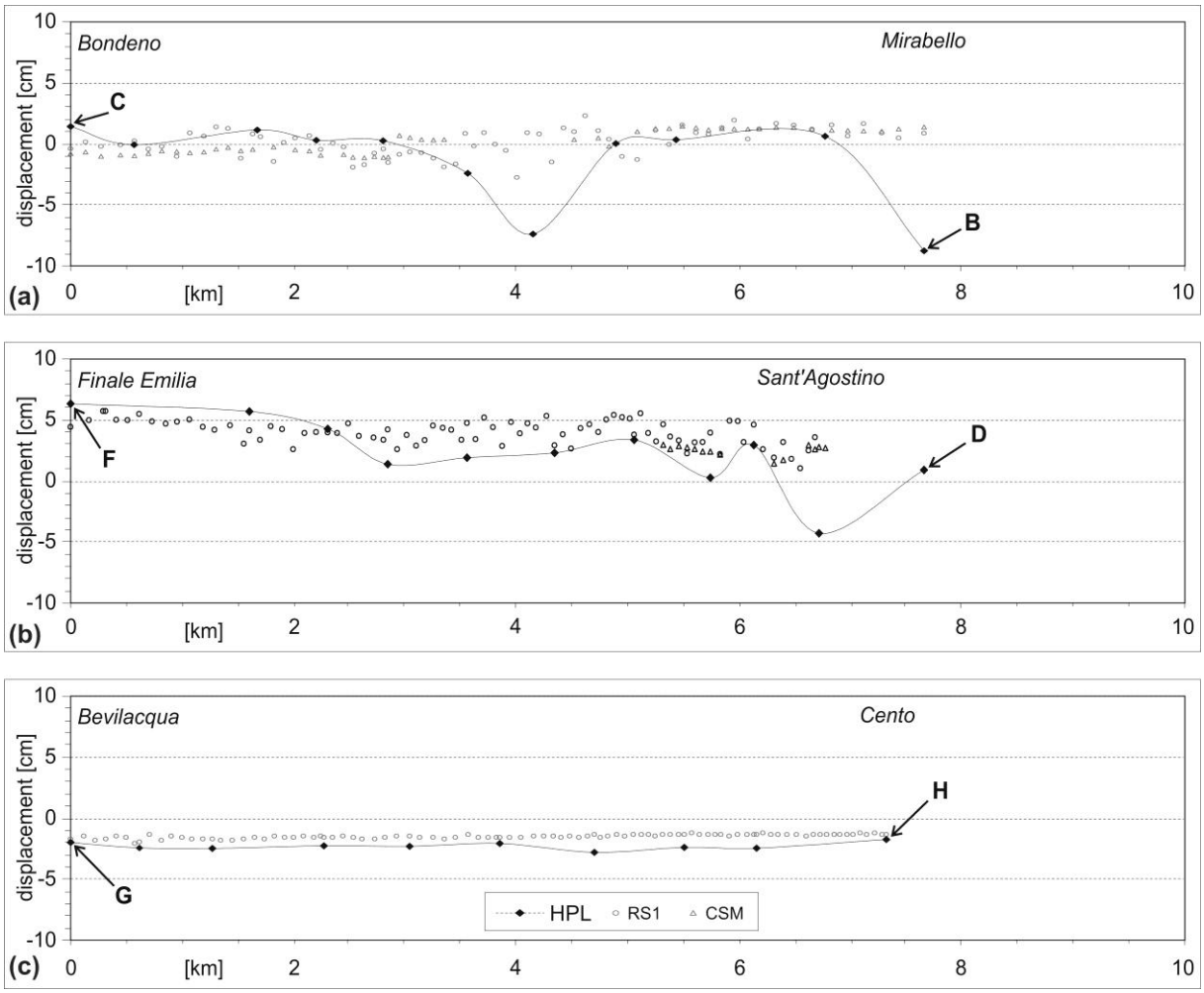

589

590

591 Figure 6

592

593

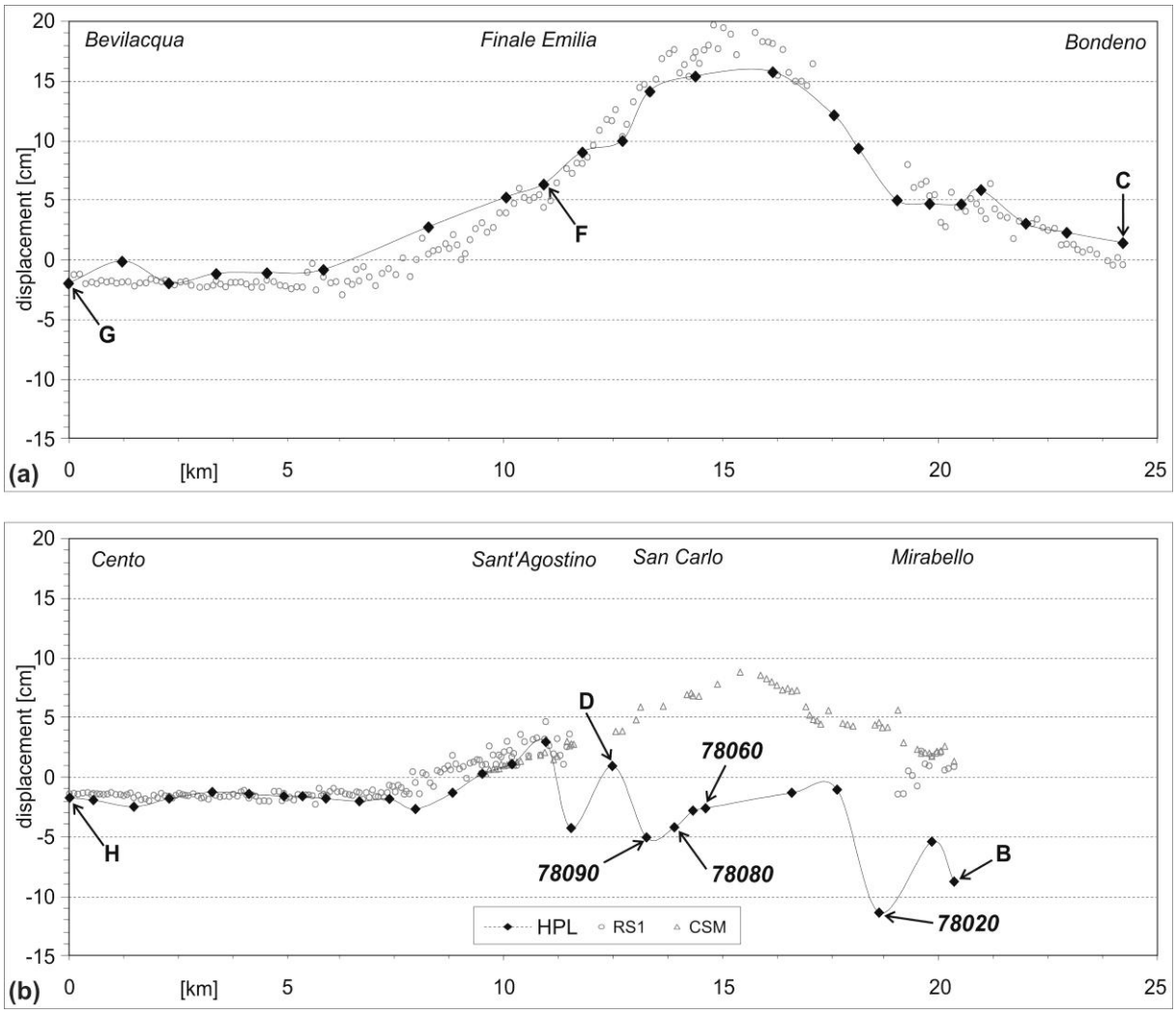

594

595

596 Figure 7

597

598

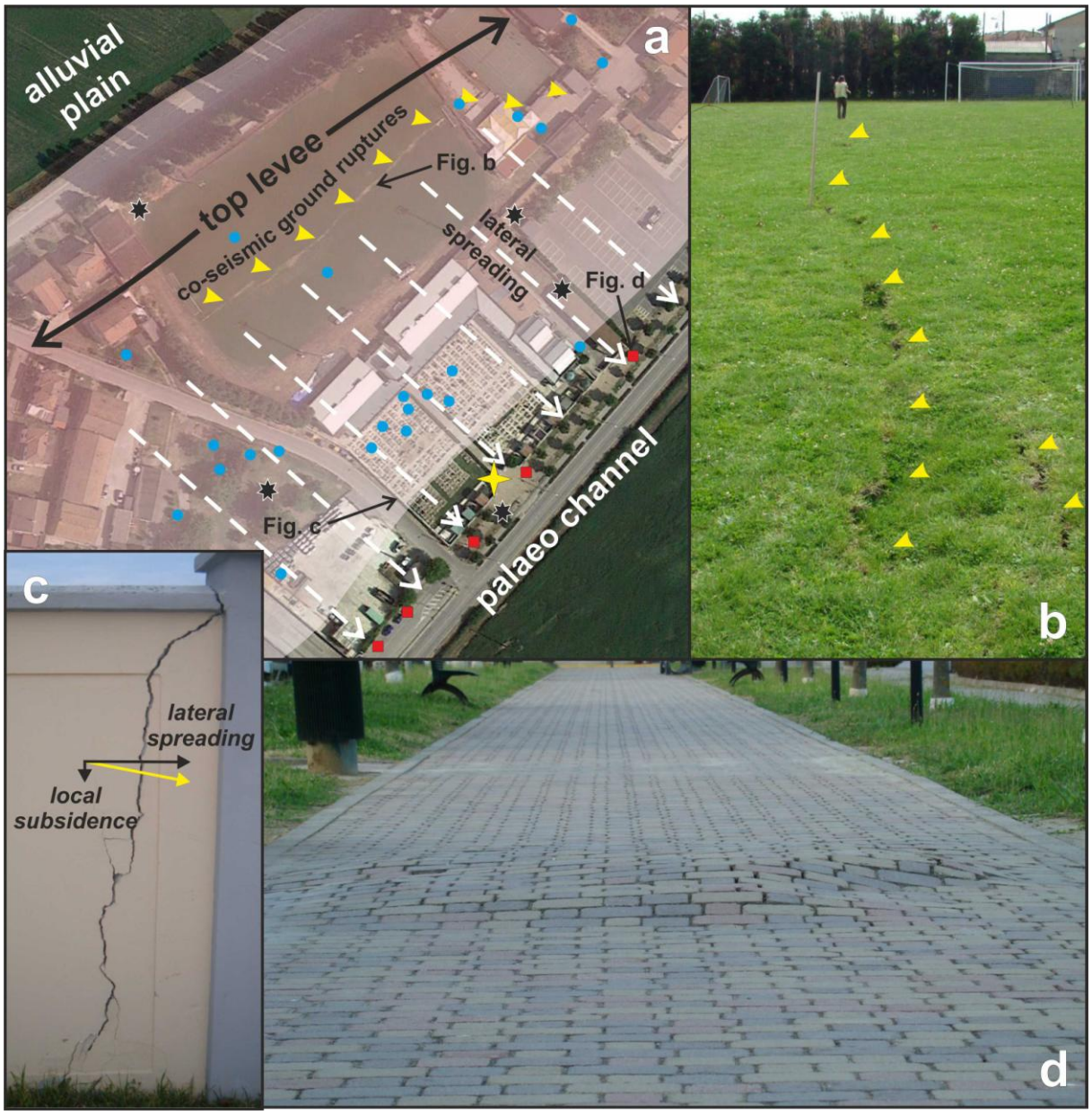

599

600

601 Figure 8

602

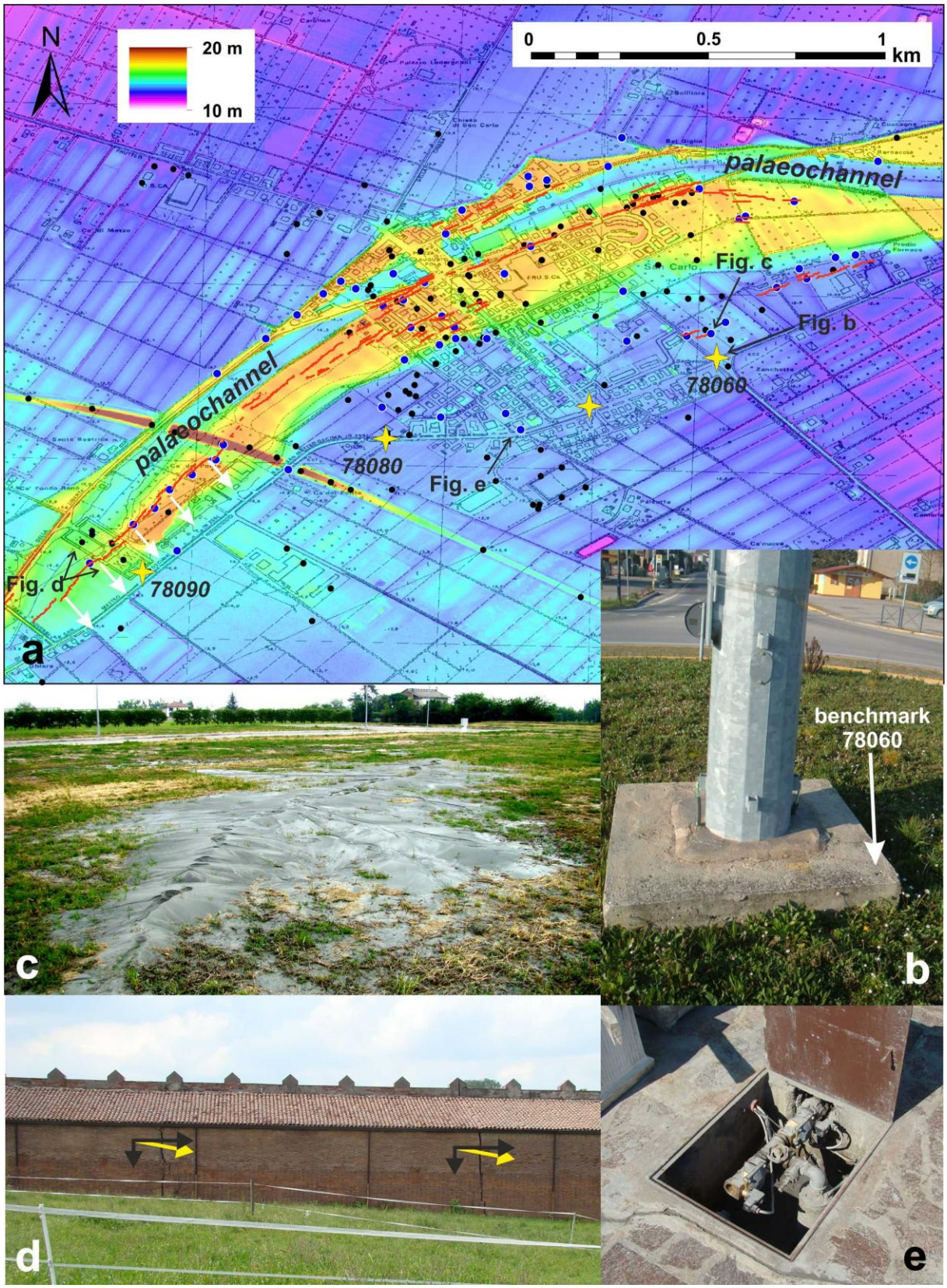
N
20 m
10 m
0
0.5
1
km
palaeochannel
palaeochannel
Fig. c
Fig. b
78060
78080
Fig. e
Fig. d
78090
a
benchmark
78060
b
c
d
e

Figure 9